Mon. Not. R. Astron. Soc. **261**, 203–221 (1993)

The steady-state structure of relativistic magnetic jets

Mark R. Dubal[1] and Ornella Pantano[2]
[1] *Center for Relativity, University of Texas at Austin, Texas 78712-1081, USA*
[2] *Dipartimento di Fisica 'G. Galilei', via Marzolo 8, 35131 Padova, Italy*

Accepted 1992 September 6. Received 1992 August 20; in original form 1992 June 30

ABSTRACT

The method of characteristics is used to study the structure of steady, relativistic jets containing a toroidal magnetic field component. We assume axisymmetry and perfect conductivity for the fluid flows. Oblique, relativistic, magnetic shocks are handled using a shock-fitting procedure. The effects of the magnetic field on the collimation and propagation of the jets are studied when the external medium has a constant or decreasing pressure distribution. Our parameter study is confined to underexpanded jet flows which have an ultrarelativistic equation of state and extremely super-magnetosonic bulk velocities. The magnetic energy density, however, may range from zero to extreme dominance. These simulations are therefore relevant to compact radio jet sources which exhibit superluminal motion.

For slightly underexpanded jets propagating into a constant-pressure external medium, the jet structure is quite periodic. This periodicity is enhanced as the toroidal field strength increases and the jet is strongly pinched. Recollimation occurs whether or not a toroidal field is present.

When the jet propagates into an external medium of decreasing pressure its structure is very dependent upon the pressure gradient. For a pressure law $p \propto z^{-2}$, where z is the distance from the jet source, the periodic structure is lost. A non-magnetic jet expands freely into the external medium and eventually comes into pressure equilibrium with it. A toroidal magnetic field cannot stop the jet from expanding. When $p \propto z^{-1}$, a semi-periodic structure is regained, and again this periodicity is particularly noticeable when a strong toroidal field is present; however, the magnetic field cannot prevent the jet from expanding, although it can greatly reduce the rate at which it does so.

Key words: MHD – relativity – shock waves – methods: numerical – galaxies: active – galaxies: jets.

1 INTRODUCTION

Many observations of extragalactic radio sources show highly collimated jets of gas emanating from a central galaxy. These outflows, possibly composed of electron–proton or electron–positron relativistic plasma, sometimes exhibit apparent superluminal motions, implying relativistic bulk velocities with Lorentz factors of $\Gamma \sim 10$ (Zensus & Pearson 1987). The radiation from the jets is typically highly polarized and follows a power-law spectrum, indicating emission by the synchrotron process. This characteristic signature in turn denotes the presence of magnetic fields, which, in many cases, will play a significant role in determining the jet structure. It is well known, for example, that helical fields are capable of collimating plasma streams via the pinch effect. In the case of high-power radio jets, measurements of the X-ray emissivity indicate that the pressure of the surrounding medium alone is insufficient to confine the jet material, and therefore magnetic fields must be invoked. Moreover, with suitable magnetic field configurations, it is possible to reduce the tendency for jet disruption by Kelvin–Helmholtz and other shearing instabilities (Ferrari, Trussoni & Zaninetti 1981). This would then allow the formation of jets with lengths $\sim 10^3$ times their beam radius.

Thus it is clear that both relativistic motion and magnetic fields play dominant roles in determining the structure of astrophysical jets. For this reason, in this paper we construct jet models by solving numerically the equations of special relativistic magnetohydrodynamics (MHD). Our models necessarily have a number of simplifying assumptions; in particular, we assume axisymmetric, adiabatic and steady flows with only a toroidal magnetic field component. These assumptions require some justification since real jets are three-dimensional, lose energy by radiative mechanisms and are turbulent to some extent.

The two-dimensional nature of our calculations is in the spirit of previous numerical jet investigations (see for example Norman & Winkler 1984; Kössl, Müller & Hillebrandt 1990a,b,c), i.e. that much can be learned from such simulations before moving on to more complex and costly three-dimensional models. Since our jet flows are stationary, we do not model instabilities, axisymmetric or otherwise, and therefore we are neglecting completely the highly unsteady sheath that appears in the dynamical simulations of Norman & Winkler and others. Sanders (1983), Wilson & Falle (1985) and Falle & Wilson (1985) have investigated some of the properties of steady hydrodynamical jets in the context of active galaxies. Close to the jet source (or nozzle), steady flow is thought to be a good approximation and therefore structures similar to those seen in laboratory jets may appear. Significant portions of the jet could be steady in very high Mach number flows, where large-scale features respond slowly to pressure changes (Falle 1991). Thus our interest is in the average overall structure of the jet, i.e. the shape of the boundary and the positions of prominent features such as knots and wiggles etc. which vary slowly when compared to longitudinal-flow time-scales. Perturbation theory also indicates that highly relativistic flows are stabilized against shearing instabilities, and that the presence of a magnetic field enhances this stability still further (Ferrari et al. 1981). Such results need to be verified in the non-linear regime by the use of high-resolution time-dependent relativistic MHD codes (Dubal 1991), but for the present we take the perturbation results to indicate that an unsteady sheath (if one should form) plays a minor role in the overall jet structure. It would be interesting to test whether the steady-jet models we construct are indeed stable.

Our approach to solving the relativistic MHD equations employs the method of characteristics, which requires that the system of partial differential equations be purely hyperbolic. This means that in steady two-dimensional flow the (magnetoacoustic) Mach number must always be greater than one and no dissipative terms can be handled. The neglect of radiation losses in the jet flow is probably the most serious approximation we make. Wilson (1987b) has modelled relativistic steady jets which are supersonic along their entire length. Many shocks occur, so the gas remains very hot and an ultrarelativistic equation of state (adiabatic index $\gamma = 4/3$) is appropriate.

The method of characteristics is well suited to study the structure of steady jets (Courant & Friedrichs 1948; Anderson 1982; for astrophysical applications see Sanders 1983 and Daly & Marscher 1988). Its power lies in the fact that domains of influence and dependence are modelled precisely, and thus it is possible to treat waves and discontinuities with high accuracy and efficiency. A number of three-dimensional characteristic techniques do exist, but they are complicated and, unlike the two-dimensional case, the approach is not unique, leading to hybrid schemes which often lose the original power of the characteristic approach. We have therefore chosen to start with the simpler two-dimensional problem.

In principle, our approach can handle any (axisymmetric) magnetic field configuration, but we include only a toroidal component, h^θ, since this is the most important one for collimation of the jet material (Kössl et al. 1990c). It is probable that h^θ helps confine the jet at the nozzle exit (Wardle & Potash 1982); a large h^θ can stabilize the nozzle wall, reducing incursion of wall material into the jet and preventing fragmentation of the wall by Kelvin–Helmholtz instabilities. In addition, hosepipe motions are reduced if the toroidal field is present in a surrounding conducting sheath, while beam disruption due to pinching modes is reduced if velocities are highly relativistic. The transverse field, $h_\perp$, would therefore be larger near the nozzle and would decay as the jet expands, while the parallel field, $h_\parallel$, increases due to the shearing of $h_\perp$ and dominates far from the source region. A large $h_\parallel$ at the source can disrupt nozzle formation, thus any asymmetry in the magnetic field configuration can lead to one-sided jets (Benford 1987).

Taking into account the above discussion, we aim to model high Mach number compact jets close enough to the nozzle region that h^θ dominates, but sufficiently far that the flow is already supermagnetosonic and therefore the gravitational influence of the primary energy source (a black hole or otherwise) may be neglected.

The plan of this paper is as follows. In the next section, we derive the characteristic and compatibility equations for two-dimensional (axisymmetric), relativistic gas flows with a single toroidal magnetic field component. Following analogous work in aerodynamic nozzle design, we rewrite the equations in terms of quantities which simplify the task of numerically solving these equations via the method of characteristics. Internal shocks can occur in the jet and their trajectories must be tracked across the characteristic grid, so in Section 3 we discuss the relations between the values of the fluid variables on either side of a relativistic, magnetic, oblique shock surface. In Section 4, the numerical approach is described in detail. Section 5 presents first some tests of the numerical code and then a parameter survey of the general flow properties of the jets. In particular, we study the effect of an increasingly large toroidal magnetic field on the initial expansion of the jet in constant- and decreasing-pressure external media. Some conclusions are drawn in Section 6.

2 THE CHARACTERISTIC FORM OF THE RELATIVISTIC MHD EQUATIONS

The equations which describe the flow of a perfectly conducting, non-self-gravitating relativistic fluid in the presence of a magnetic field are (i) the conservation of baryons, (ii) the conservation of energy-momentum and (iii) Maxwell's equations. These

may be written down as

$$\nabla_\alpha(\rho u^\alpha)=0, \qquad \nabla_\alpha T^{\alpha\beta}=0, \qquad \nabla_\alpha(u^\alpha h^\beta - u^\beta h^\alpha)=0 \tag{1a}$$

(e.g. Lichnerowicz 1967; Anile 1989), where ρ is the rest-mass density, u^α is the 4-velocity of the fluid, $T^{\alpha\beta}$ is the total stress–energy tensor and h^α represents the magnetic field. The symbol ∇_α denotes the covariant derivative compatible with a *flat* space–time metric $g^{\alpha\beta}$. For a perfect (non-viscous) fluid, the total stress–energy tensor takes the following form:

$$T^{\alpha\beta}=(e+p+\mu|h|^2)u^\alpha u^\beta+[p+(1/2)\mu|h|^2]g^{\alpha\beta}-\mu h^\alpha h^\beta, \tag{1b}$$

where p is the isotropic fluid pressure, e is the total fluid energy density, μ is the magnetic permeability and $|h|^2=h_\alpha h^\alpha>0$. Note that the magnetic field is defined such that $u^\alpha h_\alpha=0$, i.e. h^α is orthogonal to the fluid 4-velocity. The quantities ρ, p and e are all measured in the fluid comoving frame. We are assuming isotropy and infinite conductivity of the fluid, so that the conductivity $\sigma^{\alpha\beta}=\sigma_0 g^{\alpha\beta}$ with $\sigma_0\to\infty$ and the field is frozen into the fluid. The speed of light is taken to be unity.

To complete the system of equations (1), we need to add an appropriate equation of state of the form

$$p=p(e, S), \tag{2}$$

where S is the specific entropy. From Anile & Pennisi (1985), the system (1) may be manipulated to give

$$e'_p u^\alpha\nabla_\alpha p+(e+p)\nabla_\alpha u^\alpha=0, \tag{3a}$$

$$u^\alpha\nabla_\alpha S=0, \tag{3b}$$

$$u^\alpha\nabla_\alpha h^\beta - h^\alpha\nabla_\alpha u^\beta+(u^\beta h^\alpha - e'_p h^\beta u^\alpha)\frac{\nabla_\alpha p}{(e+p)}=0, \tag{3c}$$

$$(e+p+\mu|h|^2)u^\alpha\nabla_\alpha u^\beta-\mu h^\alpha\nabla_\alpha h^\beta+(g^{\alpha\beta}+2u^\alpha u^\beta)\mu h_\nu\nabla_\alpha h^\nu \tag{3d}$$

$$+\frac{1}{(e+p)}[(e+p)g^{\alpha\beta}+(e+p-e'_p\mu|h|^2)u^\alpha u^\beta+\mu h^\alpha h^\beta]\nabla_\alpha p=0,$$

$$u^\alpha u^\beta\nabla_\alpha h_\beta+\nabla_\alpha h^\alpha=0, \tag{3e}$$

where

$$e'_p=(\partial e/\partial p)_S=1/v_S^2 \qquad \text{and therefore} \qquad e'_p-1=(1-v_S^2)/v_S^2=1/c_S^2. \tag{4}$$

Here, v_S is the thermal sound speed of the fluid and $c_S=\Gamma_S v_S$, where $\Gamma(v)=(1-v^2)^{-1/2}$ is the usual special relativistic Lorentz factor.

In this paper, we will use a cylindrical coordinate system (t, r, θ, z), but consider only steady, $(\partial/\partial t=0)$, axisymmetric jets (i.e. no θ-dependence) with a single toroidal magnetic field component h^θ. Thus we can write $u^\alpha=\Gamma(1, v^r, 0, v^z)$ and $h^\alpha=(0, 0, h^\theta, 0)$, since $u^\alpha h_\alpha=0$. In this case, there is never a time component of h^α. The system of equations (3) then produces, first from (3a),

$$e'_p\left(v^r\frac{\partial p}{\partial r}+v^z\frac{\partial p}{\partial z}\right)+(e+p)\left\{\frac{\partial v^r}{\partial r}+\frac{\partial v^z}{\partial z}+\frac{v^r}{r}+\Gamma^2\left[(v^r)^2\frac{\partial v^r}{\partial r}+v^r v^z\left(\frac{\partial v^r}{\partial z}+\frac{\partial v^z}{\partial r}\right)+(v^z)^2\frac{\partial v^z}{\partial z}\right]\right\}=0, \tag{5a}$$

and secondly from (3b),

$$v^r\frac{\partial S}{\partial r}+v^z\frac{\partial S}{\partial z}=0. \tag{5b}$$

The t, r and z components of equation (3c) are identically zero, while the θ component gives

$$v^r\frac{\partial h^\theta}{\partial r}+v^z\frac{\partial h^\theta}{\partial z}-\frac{e'_p h^\theta}{(e+p)}\left(v^r\frac{\partial p}{\partial r}+v^z\frac{\partial p}{\partial z}\right)=0. \tag{5c}$$

The r and z components of equation (3d) can be manipulated, using the t component, to produce

$$w\Gamma^2\left(v^r\frac{\partial v^r}{\partial r}+v^z\frac{\partial v^r}{\partial z}\right)+\mu h_\theta\frac{\partial h^\theta}{\partial r}+\frac{\partial p}{\partial r}=0 \tag{5d}$$

and

$$w\Gamma^2\left(v^r\frac{\partial v^z}{\partial r}+v^z\frac{\partial v^z}{\partial z}\right)+\mu h_\theta\frac{\partial h^\theta}{\partial z}+\frac{\partial p}{\partial z}=0 \tag{5e}$$

respectively. Note that equation (3e) is satisfied trivially. In equations (5d) and (5e), we have written $w=e+p+\mu(h^\theta)^2$, which is the relativistic enthalpy of the fluid plus the magnetic contribution. Equation (5b) indicates that the fluid motion is adiabatic, but this condition is satisfied trivially by our choice of a perfect fluid equation of state, and therefore (5b) can be discarded. This does introduce a small error at strong shock fronts (Sanders 1983), but for weak or moderate shocks it is quite accurate. The remaining equations of the system (5) need to be solved for the unknown quantities p, h^θ, v^r and v^z. In order to achieve this, they will be written as compatibility equations holding along characteristic curves.

We first look for combinations of (5) such that the new system has the form

$$\frac{\partial \boldsymbol{U}}{\partial z}+\mathbf{A}\cdot\frac{\partial \boldsymbol{U}}{\partial r}+\boldsymbol{B}=0, \tag{6}$$

where the state vector $\boldsymbol{U}^{\mathrm{T}}=(p, h^\theta, v^r, v^z)$. We find that

$$\mathbf{A}=\begin{pmatrix}(1+1/B)v^r/v^z & (\mu h^\theta/B)v^r/v^z & w\Gamma^2v^z/B & -w\Gamma^2v^r/B\\ Cv^r/v^z & [1+(A-1)/B]v^r/v^z & Cw\Gamma^2v^z & -Cw\Gamma^2v^r\\ 1/(w\Gamma^2v^z) & \mu h^\theta/(w\Gamma^2v^z) & v^r/v^z & 0\\ -v^r/(wBc_{\mathrm{S}}^2) & -\mu h^\theta v^r/(wBc_{\mathrm{S}}^2) & -A/B & \Gamma^2v^rv^z/(Bc_{\mathrm{S}}^2)\end{pmatrix} \tag{7}$$

and

$$\boldsymbol{B}^{\mathrm{T}}=\left(\frac{w}{Br}\Gamma^2v^rv^z, \frac{Cw}{r}\Gamma^2v^rv^z, 0, -\frac{A}{Br}v^r\right), \tag{8}$$

where

$$A=\Gamma_{\mathrm{S}}^2\frac{c_{\mathrm{A}}^2}{c_{\mathrm{S}}^2}+1, \qquad B=\frac{(\Gamma v^z)^2}{c_{\mathrm{S}}^2}-A, \qquad C=\frac{(A-1)}{B\mu h^\theta}. \tag{9}$$

In the expression for A, we have defined the quantity $c_{\mathrm{A}}=\Gamma_{\mathrm{A}}v_{\mathrm{A}}$, where

$$v_{\mathrm{A}}=[\mu(h^\theta)^2/w]^{1/2}, \tag{10}$$

which is the relativistic Alfvén wave velocity in the rest frame of the fluid (see Sloan & Smarr 1987; Appl & Camenzind 1988).

The eigenvalues of the matrix **A** are found to be the double root

$$\lambda_0=\frac{v^r}{v^z}, \tag{11}$$

representing the Alfvén and slow magnetoacoustic waves, and

$$\lambda_\pm=\frac{M^rM^z\pm\sqrt{AM^2-A^2}}{(M^z)^2-A}, \tag{12}$$

representing the fast magnetoacoustic waves. Here, M^i is the relativistic Mach number defined by $M^i=\Gamma v^i/c_{\mathrm{S}}$, and $M^2=M^iM_i$. The system (6) is now rewritten as

$$\boldsymbol{l}_i\cdot\frac{\partial \boldsymbol{U}}{\partial z}+\lambda_i\boldsymbol{l}_i\cdot\frac{\partial \boldsymbol{U}}{\partial r}+\boldsymbol{l}_i\cdot\boldsymbol{B}=0, \qquad i=0,\pm, \tag{13}$$

where $\boldsymbol{l}_i$ denotes the left eigenvectors which are found by solving $\boldsymbol{l}_i\cdot\mathbf{A}=\lambda_i\boldsymbol{l}_i$. From (7), the left eigenvectors are first found to be, using (12),

$$\boldsymbol{l}_\pm=\left(1, \mu h^\theta, \pm\frac{Aw\Gamma^2v^z}{\sqrt{AM^2-A^2}}, \mp\frac{Aw\Gamma^2v^r}{\sqrt{AM^2-A^2}}\right), \tag{14}$$

and then, from (11) (since λ_0 is a double root, there are two eigenvectors associated with this solution), we find

$$\boldsymbol{l}_0^{\mathrm{I}}=\left(0,\frac{A\mu h^\theta}{(A-1)\Gamma^2 v^z w},\frac{v^r}{v^z},1\right),\qquad \boldsymbol{l}_0^{\mathrm{II}}=\left(\frac{A}{\Gamma^2 v^z w},0,\frac{v^r}{v^z},1\right). \tag{15}$$

The compatibility equations are then

$$\boldsymbol{l}_i\cdot\mathrm{d}\boldsymbol{U}+\boldsymbol{l}_i\cdot\boldsymbol{B}\,\mathrm{d}z=0 \qquad \text{along} \qquad \frac{\mathrm{d}r}{\mathrm{d}z}=\lambda_i. \tag{16}$$

From (16), for the case of $\lambda_i=\lambda_\pm$ we have

$$\mathrm{d}p+\mu h^\theta\,\mathrm{d}h^\theta\pm\frac{Aw\Gamma^2 v^z}{\sqrt{AM^2-A^2}}\mathrm{d}v^r\mp\frac{Aw\Gamma^2 v^r}{\sqrt{AM^2-A^2}}\mathrm{d}v^z+\frac{Aw\Gamma^2}{B}\left[v^z\pm\frac{Av^r}{\sqrt{AM^2-A^2}}\right]\frac{v^r}{r}\mathrm{d}z=0, \tag{17}$$

which are satisfied along the characteristic curve

$$\frac{\mathrm{d}r}{\mathrm{d}z}=\frac{M_r M_z\pm\sqrt{AM^2-A^2}}{B}, \tag{18}$$

while for $\lambda_i=\lambda_0$, we obtain

$$\mathrm{I}\qquad \frac{A\mu h^\theta}{(A-1)\Gamma^2 v^z w}\mathrm{d}h^\theta+\frac{v^r}{v^z}\mathrm{d}v^r+\mathrm{d}v^z=0 \tag{19}$$

and

$$\mathrm{II}\qquad \frac{A}{\Gamma^2 v^z w}\mathrm{d}p+\frac{v^r}{v^z}\mathrm{d}v^r+\mathrm{d}v^z=0, \tag{20}$$

which both hold along the characteristic curve

$$\frac{\mathrm{d}r}{\mathrm{d}z}=\frac{v^r}{v^z}. \tag{21}$$

If we had included equation (5b) in the scheme, then λ_0 would have been a triple root with the third solution giving $\mathrm{d}S=0$ along the streamline (21).

At this point, equations (17)–(21) may be written in a form more suitable for a numerical solution. Following Courant & Friedrichs (1948) (see also Sanders 1983; Anderson 1985; Daly & Marscher 1988), we write the fluid 3-velocity components as

$$v^r=V\sin\Theta,\qquad v^z=V\cos\Theta, \tag{22}$$

where Θ is the angle between the velocity vector of magnitude V and the symmetry axis (z-axis) of the jet. We also introduce the relativistic Mach angle, μ, defined by

$$\sin\mu=1/M. \tag{23}$$

For the magnetic flows considered here, however, it is more convenient to use a modified version of this, which is given by

$$\sin^2\xi=A\,\sin^2\mu. \tag{24}$$

We note from (18) that in order for the characteristics to be real (i.e. for the system to be hyperbolic) we must have $M^2\geq A$ or equivalently $|\sin\xi|\leq 1$, and therefore the substitution (24) is valid for the purposes of the solution method described here. This is just the condition that the flow be supermagnetosonic in order to maintain a hyperbolic system. Substituting (22) and (24) into equations (17)–(21) produces the following compatibility equations:

$$\mathrm{d}p+\frac{1}{2}\mu\,\mathrm{d}H+w(\Gamma^2-1)\tan\xi\left[\left(\frac{1}{\cot\xi\pm\cot\Theta}\right)\mathrm{d}\ln r\pm\mathrm{d}\Theta\right]=0, \tag{25}$$

holding along the C^+ and C^- curves

$$\frac{\mathrm{d}r}{\mathrm{d}z}=\tan(\Theta\pm\xi), \tag{26}$$

and

$$\text{I} \qquad \frac{A}{2(A-1)w}\mu\, \mathrm{d}H + \mathrm{d}\ln\Gamma = 0, \tag{27}$$

$$\text{II} \qquad \frac{A}{w}\mathrm{d}p + \mathrm{d}\ln\Gamma = 0, \tag{28}$$

holding along the streamline

$$\frac{\mathrm{d}r}{\mathrm{d}z} = \tan\Theta, \tag{29}$$

where $H = (h^{\theta})^2$.

By combining equations (27) and (28), it is possible to obtain a generalization of the relativistic Bernoulli equation when a magnetic field is present:

$$p_*^{p_*/w}\Gamma = \text{constant along a streamline}, \tag{30}$$

where $p_* = p + (\mu H)/2$ is the effective total pressure.

3 JUNCTION CONDITIONS AT AN OBLIQUE SHOCK FRONT

If the ratio of the jet pressure to the external pressure is sufficiently high or low, then internal shocks will occur. Since the characteristic method cannot 'capture' shocks, it is necessary to use a shock-fitting scheme. For this, we require the relations between fluid variables on either side of the shock region. These are given by the following jump conditions:

$$[\rho u^{\alpha}]N^{\alpha} = 0, \tag{31}$$

$$[T^{\alpha\beta}]N^{\alpha} = 0 \tag{32}$$

and

$$[u^{\alpha}h^{\beta} - u^{\beta}h^{\alpha}]N^{\alpha} = 0 \tag{33}$$

(Lichnerowicz 1967), where $[Z]$ denotes the jump in the quantity Z across the shock and N_{α} are the components of the unit 4-vector normal to the shock surface. If we call ψ the angle between the shock normal and the positive z-direction (see Fig. 1), then the components of N_{α} are

$$N_{\alpha} = (0, \sin\psi, 0, \cos\psi). \tag{34}$$

The configurations considered in this paper are such that the magnetic field always acts transversely to the direction of propagation of the shock surface, i.e.

$$h^{\alpha}N_{\alpha} = 0. \tag{35}$$

Thus in our case the system (31)–(33) reduces to the following:

$$\rho_{\mathrm{u}}\Gamma_{\mathrm{u}}v_{\mathrm{u}\perp} = \rho_{\mathrm{s}}\Gamma_{\mathrm{s}}v_{\mathrm{s}\perp}; \tag{36}$$

$$w_{\mathrm{u}}\Gamma_{\mathrm{u}}^2 v_{\mathrm{u}\perp} = w_{\mathrm{s}}\Gamma_{\mathrm{s}}^2 v_{\mathrm{s}\perp}; \tag{37}$$

$$w_{\mathrm{u}}\Gamma_{\mathrm{u}}^2 v_{\mathrm{u}\perp}^2 + p_{\mathrm{u}} + (\mu H_{\mathrm{u}})/2 = w_{\mathrm{s}}\Gamma_{\mathrm{s}}^2 v_{\mathrm{s}\perp}^2 + p_{\mathrm{s}} + (\mu H_{\mathrm{s}})/2; \tag{38}$$

$$w_{\mathrm{u}}\Gamma_{\mathrm{u}}^2 v_{\mathrm{u}\perp} v_{\mathrm{u}\parallel} = w_{\mathrm{s}}\Gamma_{\mathrm{s}}^2 v_{\mathrm{s}\perp} v_{\mathrm{s}\parallel}, \tag{39}$$

and

$$h_{\mathrm{u}}^{\theta}\Gamma_{\mathrm{u}} v_{\mathrm{u}\perp} = h_{\mathrm{s}}^{\theta}\Gamma_{\mathrm{s}} v_{\mathrm{s}\perp}, \tag{40}$$

where $v_{\perp}$ and $v_{\parallel}$ are the velocity components perpendicular and parallel to the shock surface, respectively. The unshocked values of the fluid variables (upstream of the shock) are indicated by the subscript u, while the subscript s is used for the shocked values. The component of fluid velocity parallel to the shock surface must be continuous across the shock, as can be easily verified by combining equations (37) and (39). For a stable shock, on the other hand, the normal component of velocity must

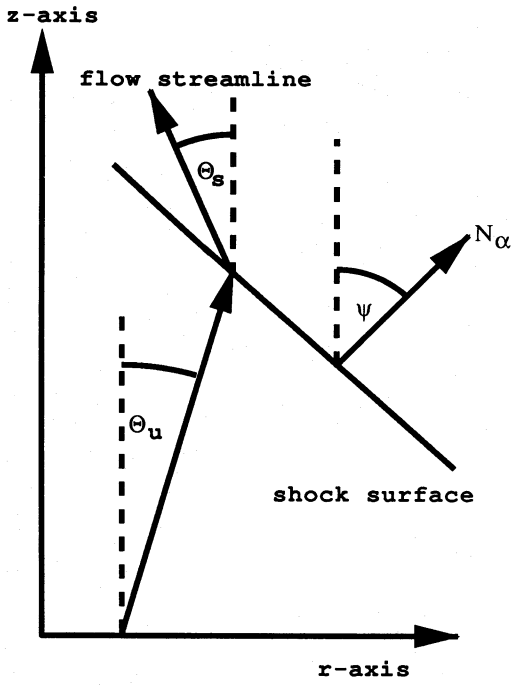

Figure 1. Flow geometry at an incident oblique shock. See the text for details.

decrease across it; so, as in Königl (1980), we introduce the quantity

$$\chi=\frac{v_{s\perp}}{v_{u\perp}}=\frac{\tan(\psi-\Theta_u)}{\tan(\psi-\Theta_s)}\le 1, \tag{41}$$

which provides a measure of the shock strength.

For the purpose of numerical integration, it is convenient to rewrite equations (36)–(40) such that the shocked values are expressed only in terms of the upstream values and the angle ψ. Assuming an ultrarelativistic (barotropic) equation of state, $p=(\gamma-1)e$, we obtain a quadratic for χ, with solutions

$$\chi=Y\left[1\pm\sqrt{1+\frac{(2-\gamma)\mu H_u}{Y\gamma[p_u+(\mu H_u)/2]}}\right] \tag{42}$$

where

$$Y=\frac{\gamma[p_u+(\mu H_u)/2](\Gamma_u^2 v_{u\perp}^2+1)}{2w_u\Gamma_u^2 v_{u\perp}^2}, \qquad \Gamma_u^2 v_{u\perp}^2=\frac{(\Gamma_u^2-1)(1+\tan\psi\tan\Theta_u)^2}{(1+\tan^2\psi)(1+\tan^2\Theta_u)}.$$

From (42), we see that only the plus sign provides a physical solution, in which case

$$\tan\Theta_s=\frac{\chi\tan\psi(1+\tan\psi\tan\Theta_u)-(\tan\psi-\tan\Theta_u)}{\tan\psi(\tan\psi-\tan\Theta_u)+\chi(1+\tan\psi\tan\Theta_u)}, \tag{43}$$

$$\Gamma_s=\frac{\Gamma_u}{\sqrt{1+\Gamma_u^2 v_{u\perp}^2(1-\chi^2)}}, \tag{44}$$

$$h_s^\theta=\frac{h_u^\theta}{\chi}\sqrt{1+\Gamma_u^2 v_{u\perp}^2(1-\chi^2)}, \tag{45}$$

$$p_s=[1+\Gamma_u^2 v_{u\perp}^2(1-\chi^2)]\left[\frac{p_u}{\chi}-\frac{(\gamma-1)(1-\chi)}{\gamma\chi^2}\mu H_u\right]. \tag{46}$$

Given the conditions of the flow upstream of the shock it is clear that, once ψ is known, all quantities on the downstream side can be found. However, to determine ψ, information from the downstream side of the shock must be provided. This information is obtained via the C^- or C^+ curves, depending on whether the shock is incident or reflected. Further details and a description of the numerical procedure adopted are given in the next section.

Figs 2 and 3 show solutions of the jump conditions (42)–(46) when $\gamma = 4/3$. The parts of the figures show logarithmic contour plots of (a) the downstream Mach number and (b) the thermal pressure jump, p_s/p_u, for the upstream Mach number between 1 and 50 and the shock angle $\delta = \psi - \Theta_u$ between 0° and 90°. In the case of Fig. 2, no magnetic field is present (hydrodynamical shocks), while for Fig. 3 the upstream thermal and magnetic pressures are equal [i.e. $p_u = (\mu H_u)/2$]. The magnetic field jump, h_s^θ/h_u^θ, is qualitatively identical to the pressure jump.

Since we are using the method of characteristics, it is necessary for the flow to be supermagnetosonic (i.e. $M^2 > A$) everywhere. The shaded region on the left of the figures is where this condition is not satisfied. Apart from slightly supersonic upstream flows, the transition from super to submagnetosonic flows occurs at almost constant values of shock angle; these being $\delta = 30°$ and $\delta = 45°$ for Figs 2 and 3 respectively. It is interesting to note that, once the upstream flow is moderately supersonic, e.g. $M \geq 4$, the downstream Mach number is essentially only a function of the shock angle δ. Unless the shocks are quite oblique,

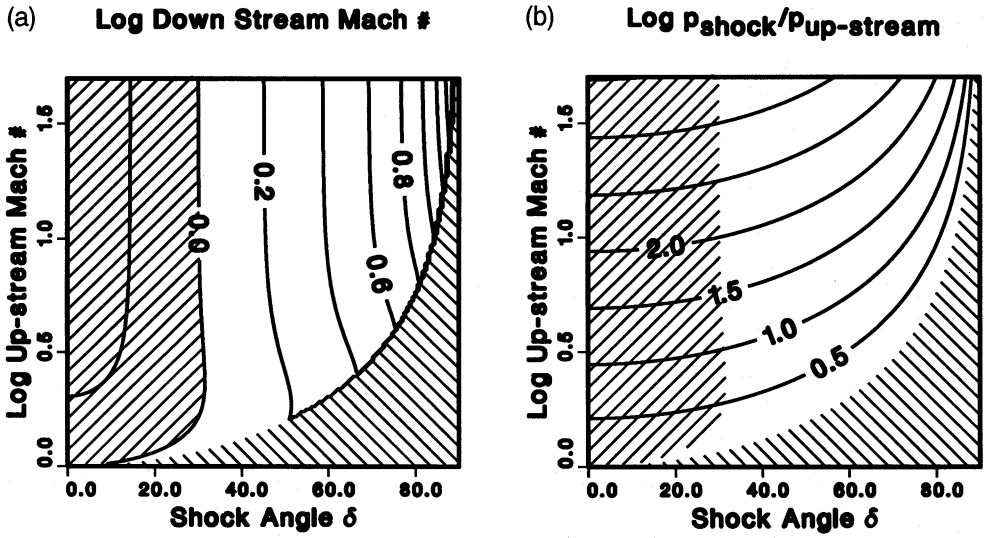

Figure 2. Logarithmic contour plots of (a) the post-shock Mach number and (b) the pressure jump, for a range of upstream Mach numbers and shock angles when $\gamma = 4/3$. In this case, no magnetic field is present. The shaded area on the left denotes the region where the characteristics are no longer real, i.e. $M^2 \leq A$, and which is therefore not accessible using our numerical method. The shaded region on the right is where $\chi > 1$ and so does not correspond to shock solutions.

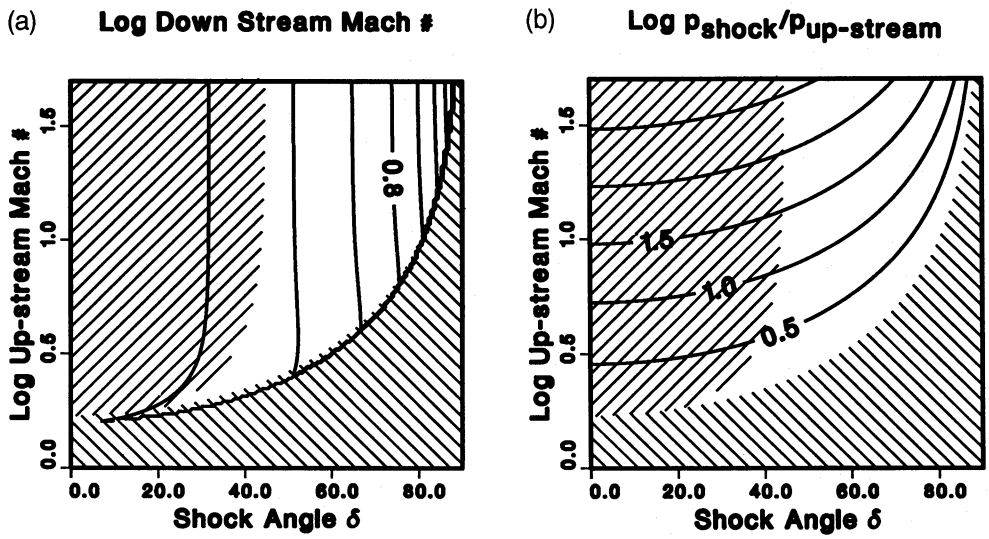

Figure 3. Same as Fig. 2 except that the upstream thermal and magnetic pressures are equal.

the bulk fluid velocity can be reduced very substantially. For example, a fluid with an initial Mach number of 20 passing through a shock with $\delta = 60°$ has a final Mach number of ~ 2.5, if no magnetic field is present. For equal thermal and magnetic pressures, the final Mach number is higher at ~ 3.5 (and is increasing for increasing field strength); nevertheless, it is still substantially reduced. This does not, of course, take account of jet expansion, which, for a supersonic flow, would increase the velocity. However, if the jet is well collimated, at least near the nozzle as we assume, then no such speed-up would occur. This suggests that, in order for a jet to form and progress into the surrounding medium, close to the nozzle there are either no shocks present or they are very weak or very oblique. A very small number (two or three) of moderately perpendicular shocks ($\delta < 60°$) would rapidly disrupt the progress of the jet due to the flow becoming subsonic and turbulent. For an increasing magnetic field, the shock strength (as measured by the ratio p_s/p_u) decreases. This is due to a stiffening of the jet fluid, since it behaves with an effective adiabatic index $\gamma \to 2$ as the field increases. This is because the magnetoacoustic and Alfvén wave speeds approach the velocity of light. It then becomes increasingly difficult to produce strong shocks (see De Hoffman & Teller 1950; Kennel & Coroniti 1984; Appl & Camenzind 1988). Thus the toroidal magnetic field could have a number of vital roles in the production and propagation of the jet. First, the toroidal field helps to form the nozzle itself; secondly, it can reduce the tendency of nozzle breakup due to fluid instabilities, and thirdly, a strong toroidal field can inhibit the formation of strong shocks, which could otherwise cause a rapid termination of the jet. Since the toroidal field strength appears to be a crucial factor, any significant asymmetries in the field configuration can easily lead to one-sided sources (Benford 1987).

When $\chi > 1$, the fluid velocity component normal to the shock front is not supermagnetosonic and therefore a shock cannot form. This condition is indicated by the shaded region on the right-hand side of Figs 2 and 3. The boundary of the region at $\chi = 1$ corresponds to the solution $\log(p_s/p_u) = 0$.

4 NUMERICAL SOLUTION METHOD

The system (25)–(29) is a set of seven equations which must be solved for the unknown variables p, Θ, H and Γ on a grid constructed from characteristic curves, i.e. the grid itself must be obtained as part of the solution. We will outline the salient features of the numerical procedure adopted to do this since, although the techniques are well known in engineering fluid dynamics, they may not be familiar to many astrophysicists. Moreover, there are a number of novel features in our problem which make the integration procedure somewhat non-standard, in particular the presence of the magnetic field and the fact that we will integrate along the streamlines in addition to the forward and backward characteristic curves.

The basic techniques described here are similar to those used in jet-nozzle design (see e.g. Hoskin 1963; Owczarek 1964; Anderson 1982, 1985), except that in this case the outer boundary is a free surface rather than a wall. There are primarily four different types of grid point: (i) an internal point; (ii) an axis point; (iii) a free surface point, and (iv) a shock point, shown in Figs 4(a)–(d) respectively. We will consider the treatment of each type of point in turn.

4.1 Internal points

Since the system is hyperbolic, the equations are integrated in the z-direction (taken to be a pseudo time) from an initial $r =$ constant Cauchy slice. Consider the situation shown in Fig. 4(a), in which the filled circles represent grid points at which the data are known. The goal is to use these data to compute not only the unknowns at the new grid points (open circle), but also the positions of such points. This requires the use of an iterative procedure. First, the position of point 3 in Fig. 4(a) is determined by the intersection of the C^+ and C^- characteristic curves from points 1 and 2 respectively, the slopes of which are given by equation (26). We will approximate the characteristic curves between adjacent grid points by straight lines. This approach gives rise to a numerical scheme with first-order convergence properties (see subsection 5.1). Referring to Fig. 4(a), it is also necessary for the streamline to pass through grid point 3, and therefore initial data must be interpolated from points 1 and 2 to a point 4 where the base of the streamline intersects a line joining 1 and 2. For a first-order scheme, a simple linear interpolation method is adequate for this purpose. Thus, at the general point 3, all seven equations need to be solved together iteratively to find p_3, Θ_3, H_3, Γ_3, r_3, z_3 and r_4, where the subscript refers to the grid-point numbers shown in Fig. 4(a).

The equations (25)–(29) are finite-differenced in a very simple way, e.g. from (26) the C^+ curve from 1 to 3 is written as

$$r_3 - r_1 = [\tan(\Theta_3 + \xi_3) + \tan(\Theta_1 + \xi_1)](z_3 - z_1)/2 \tag{47}$$

and from (25) the equation holding along this curve is written as

$$(p_3 - p_1) + \frac{1}{2}\mu(H_3 - H_1) + \frac{1}{2}\left[\frac{w_3(\Gamma_3^2 - 1)\tan\xi_3}{\cot\xi_3 + \cot\Theta_3} + \frac{w_1(\Gamma_1^2 - 1)\tan\xi_1}{\cot\xi_1 + \cot\Theta_1}\right]\ln\left(\frac{r_3}{r_1}\right) \tag{48}$$

$$+ \frac{1}{2}[w_3(\Gamma_3^2 - 1)\tan\xi_3 + w_1(\Gamma_1^2 - 1)\tan\xi_1](\Theta_3 - \Theta_1) = 0.$$

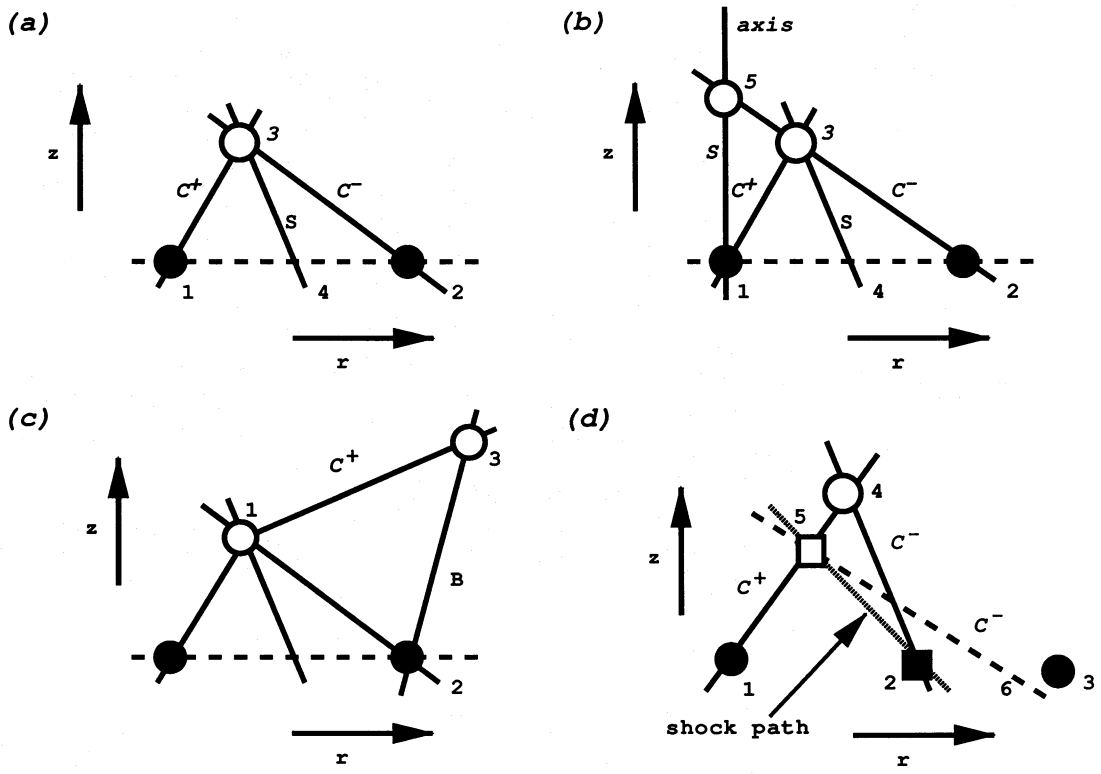

Figure 4. Calculation of data at the four different types of grid point occurring during the integration. The filled black areas denote points at which the data are known; open areas are points at which data are to be determined. (a) Calculation of data at an internal point 3. $C^{\pm}$ are the forward and backward characteristics from point 3 and S is the streamline passing through 3. The foot of the streamline is at point 4. (b) Computation of axis points. Data points 3 and 5 require special treatment due to the axis singularity. (c) Computation of jet boundary points. The streamline B (2→3) is the jet's surface. (d) Propagation of the known shock point 2 (shown as a black square) through the grid. Point 5 is determined using the shock angle $\delta = \psi - \theta_u$ at 2. The curve 6→5 is an interpolated backward characteristic from the new shock point (white square).

The other equations are differenced in a similar way. With initial estimates for the unknowns, the coupled non-linear algebraic equations can be solved at each grid point using the MINPACK iteration routine HYBRD1; this has proved to be an efficient solution method.

4.2 Axis points

The jets are axisymmetric, so the z-axis is a coordinate singularity and special treatment is required for equation (25). There are two possible situations to consider: (a) when the data at the axis point are known and are being used to propagate data forward, or (b) when the data are to be computed on the axis point. Fig. 4(b) shows both situations, which occur alternately as we integrate in the z-direction. In case (a), the equation holding along the C^+ characteristic curve from point 1 must be modified. Consider the term d ln r/(cot ξ + cot Θ) in the limit $r \to 0$. We have that $\Theta \to 0$ also, since at $r = 0$ the flow must be along the axis. Therefore

$$\lim_{r,\Theta\to 0}\left(\frac{1}{\cot\xi+\cot\Theta}\right)\frac{\mathrm{d}r}{r}=\lim_{r,\Theta\to 0}\tan\Theta\,\frac{\mathrm{d}r}{r}=\lim_{r,\Theta\to 0}\frac{\Theta}{r}\,\mathrm{d}r=\frac{\mathrm{d}\Theta}{\mathrm{d}r}\,\mathrm{d}r=\mathrm{d}\Theta. \tag{49}$$

With this modification, grid point 3 is treated in exactly the same way as an ordinary internal point described above. For case (b) (grid point 5 in Fig. 4b), due to axisymmetry not all seven equations are required. The position of the grid point is $r = 0$, with the z value to be obtained from the intersection of the C^- curve with the axis. By symmetry, the C^+ equation is the mirror image and so can be discarded. In addition, the streamline itself is known – it is simply the z-axis – and so $\Theta = 0$, which implies that equation (29) can also be discarded. Another condition on the axis concerns the magnetic field component h^θ which, in order to be non-singular, must vanish. Equation (27) is therefore discarded and $H = 0$ on the axis may be used to simplify the remaining equations. The unknown quantities at grid point 5 are then p_5, Γ_5 and z_5, and the equations used are the C^- curve from (26), its compatibility equation from (25) (which must be modified using the limit shown in equation 49), and equation (28), holding along the streamline between points 1 and 5.

4.3 Boundary points

The outer boundary is a free surface where the pressure of the external medium is specified. In principle, it is possible to specify the flow angle, Θ, rather than the pressure, so that the jet shape can be customized, leading to a particular behaviour of the external pressure gradient. This was done by Wilson (1987a), but here we will use only specified external pressure values.

The grid structure at the boundary is shown in Fig. 4(c), where the data are known at points 1 and 2, and the boundary values of Θ, H, Γ and position r, z at point 3 are to be determined. Noting that the jet boundary, curve 2 to 3, is a streamline, the equations required are the C^+ curve from 1 to 3 and its compatibility equation (from (26) and (25) respectively) and the streamline equation (27)–(29). Again, an iterative procedure is used.

4.4 Shock points

As discussed in the previous section, if the ratio of jet pressure to external pressure is sufficiently high or low, then internal shocks will occur. There are two problems to consider in the numerical treatment of these shocks: first their detection and secondly their propagation through the characteristic grid.

A shock is indicated when two characteristics of the same family, say C^+, intersect. The position of the shock point is easily determined from the slopes of the characteristic curves. At the shock point, it is then necessary to solve the relativistic Rankine–Hugoniot relations (42)–(46) along with the characteristic and compatibility equations. The shock detection and fitting procedure is essentially the same as that used to propagate a previously inserted shock point, which we now describe.

Once a shock point has been detected, it must be propagated throughout the characteristic grid. The following procedure is based on that described by Moe & Troesch (1960) and Illingworth (1953) for their Newtonian jet calculations.

Consider the situation shown in Fig. 4(d), where 1, 2 and 3 are known data points and 2 is a shock point (which is double-valued in that it carries a set of unshocked and shocked values of the fluid variables). First, point 4 is obtained from 1 and the unshocked side of 2 using the standard procedure for an internal point, as described above. From the value of the shock angle $\delta_2 = (\psi - \Theta_u)_2$ at 2, point 5 may be determined as the intersection of the shock path with the C^+ characteristic curve 1 to 4. At 5, the unshocked values Θ_u, Γ_u, p_u and H_u may be determined by interpolation between 1 and 4. To find the shocked values of the quantities and the new shock angle, it is necessary to solve the jump conditions (42)–(46) at 5 along with the C^- characteristic and compatibility equations extending back from point 5, with base values at point 6 interpolated from points 2 (shocked side) and 3. From equations (25) and (26), we have that these last two equations are

$$r_5 - r_6 = [\tan(\Theta_s - \xi_s) + \tan(\Theta_6 - \xi_6)](z_5 - z_6)/2 \tag{50}$$

and

$$(p_s - p_6) + \frac{1}{2}\mu(H_s - H_6) + \frac{1}{2}\left[\frac{w_s(\Gamma_s^2 - 1)\tan\xi_s}{\cot\xi_s - \cot\Theta_s} + \frac{w_6(\Gamma_6^2 - 1)\tan\xi_6}{\cot\xi_6 - \cot\Theta_6}\right]\ln\left(\frac{r_s}{r_6}\right) \tag{51}$$

$$-\frac{1}{2}[w_s(\Gamma_s^2 - 1)\tan\xi_s + w_6(\Gamma_6^2 - 1)\tan\xi_6](\Theta_s - \Theta_6) = 0.$$

Once again, this is an iterative procedure to find the shocked values Θ_s, Γ_s, p_s and H_s, the new shock angle $\delta_5 = (\psi - \Theta_u)_5$, and the foot of the interpolated C^- characteristic curve, r_6, z_6; a total of seven equations for seven unknowns.

5 RESULTS OF CALCULATIONS

In a constant external medium, our jet models are characterized by three parameters: α, β and M_{jet}, where

$$\alpha = \left(\frac{\text{pressure of external medium at base of jet}}{\text{initial pressure at base of jet}}\right)^{1/2} = \left(\frac{p_{ext}}{p_{jet}}\right)^{1/2},$$

$$\beta = \left(\frac{\text{largest magnetic pressure at base of jet}}{\text{initial pressure at base of jet}}\right) = \left(\frac{\mu H_{max}}{2p_{jet}}\right),$$

M_{jet} = initial Mach number of jet flow.

Note that our β is the reciprocal of the usual plasma β. For all the models shown in this paper, an ultrarelativistic equation of state, $p = (\gamma - 1)e$, with adiabatic index $\gamma = 4/3$, is used. The initial conditions at the nozzle entrance are shown in Fig. 5. In

practice, the step function at the boundary is modelled by three grid points. Given the pressure and magnetic field values on the boundary, it is possible to obtain the Lorentz factor there by using the Bernoulli relation (30) and assuming the streamline constant is approximately the same for adjacent points. The toroidal field configuration is given by

$$H = H_{\max}(r/r_{\rm patch})^2 \quad \text{if} \quad r < r_{\rm patch},$$

$$H = H_{\max}(r_{\rm patch}/r)^2 \quad \text{if} \quad r \geq r_{\rm patch},$$

where usually $r_{\rm patch} = 0.98\, r_{\rm jet}$. This configuration is similar to that used by Lind et al. (1989) in their dynamical simulations. For a typical case, the initial data line is modelled using ~ 80 grid points. As the calculation proceeds, grid points may be added if the distance between adjacent points exceeds a certain value (with linear interpolation to the new points) or deleted if they are too close. This facility is vital for the success of the characteristic method. A complete calculation may consist of more than $\sim 10^5$ data points.

5.1 Tests of the code

In order to check that the code is performing as expected, we have used the analytic expressions obtained by Daly & Marscher (1988) for the maximum radius, $r_{\max}$, and length-scale, $z_{\max}$ (the distance from the nozzle exit to the next minimum radius, see fig. 1 of Daly & Marscher 1988), for a non-magnetic supersonic jet propagating in a uniform-pressure medium. They state that

$$\frac{r_{\max}}{r_{\rm jet}} \sim 1 + 1.9 \left(\frac{1-\sqrt{\alpha}}{2\sqrt{\alpha}-1} \right) \tag{52}$$

and

$$\frac{z_{\max}}{r_{\rm jet}} \sim 3.3 \left(\frac{\Gamma_{\rm jet}}{\alpha^2} \right). \tag{53}$$

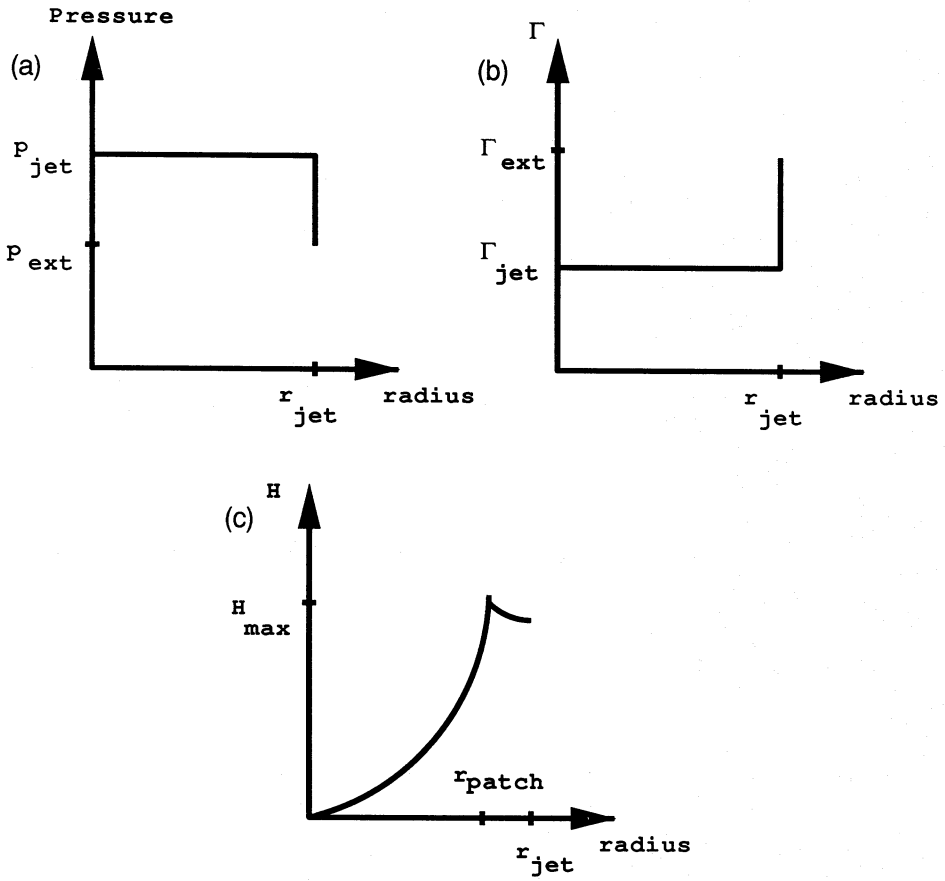

Figure 5. Input conditions at the base of the jet ($z = 0$), showing the radial profiles of (a) the thermal pressure, (b) the Lorentz factor, and (c) H.

Table 1. Test of the code using the expressions for r_{max} and z_{max} given by Daly & Marscher (1988), denoted by D-M. Here $M_{jet} = 10$ and $\beta = 0$.

$1/\alpha^2$	r_{max} D-M	r_{max} Code	Diff %	z_{max} D-M	z_{max} Code	Diff %
1.1	1.0469	1.0393	0.73	25.923	25.425	1.92
1.3	1.1382	1.1137	2.15	30.637	27.450	10.40
1.5	1.2269	1.1841	3.49	35.350	30.705	13.14
2.0	1.4434	1.3462	6.73	47.133	38.433	18.45

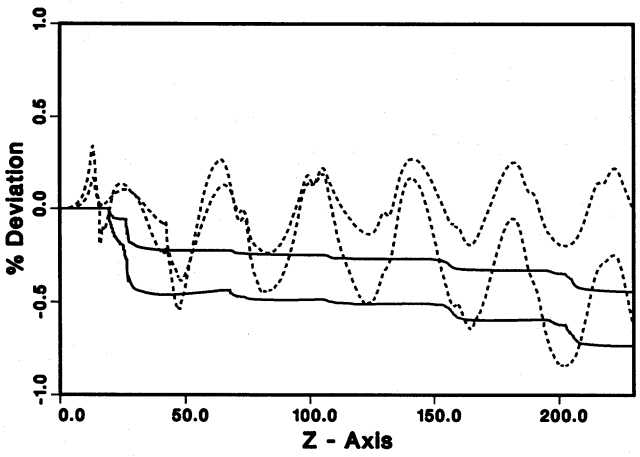

Figure 6. Consistency check on the code. The Bernoulli equation (30) is evaluated along the z-axis for $1/\alpha^2 = 1.2$ with $\beta = 0$ (solid lines) and $\beta = 1$ (broken lines) when 40 or 80 grid points are placed along the nozzle exit. The inconsistency behaves in a first-order way.

These expressions have been obtained by taking small-angle expansions in the two-dimensional (planar) characteristic equations (Daly & Marscher 1988). They are accurate for large Γ_{jet} and α close to one.

Taking $r_{jet} = 1$ and $\Gamma_{jet} = 7.14$ (corresponding to $M_{jet} = 10$), we have computed r_{max} and z_{max} for various values of α. As can be seen from Table 1, the numerical and theoretical values are close for $\alpha \sim 1$, but diverge as the pressure ratio becomes larger, as expected. Some additional discrepancy occurs because we are simulating axisymmetric jets rather than planar ones. From expression (49), we see that on the z-axis there is a factor of 2 difference in equation (11d) of Daly & Marscher between planar and axisymmetric jets. Their expression (23) for the minimum pressure is therefore invalid in our case and, indeed, we obtain significantly lower values of the minimum pressure. This would aid collimation, leading to lower values of r_{max} and z_{max}, which is consistent with our results.

A consistency check on the code is possible by making use of the Bernoulli equation (30) along the z-axis of the jet, since this is a streamline. The percentage deviation from a constant value for expression (30) is shown in Fig. 6 for two jets with $1/\alpha^2 = 1.2$, $\beta = 0$ (solid lines) and $1/\alpha^2 = 1.2$, $\beta = 1$ (broken lines), both of which have either 40 or 80 grid points across the nozzle exit. No shocks occur in these jets. It can be seen that the Bernoulli equation is satisfied to < 1 per cent in the case of 40 points and < 0.5 per cent in the case of 80 points. Thus the discretization error can be reduced by increasing the number of points in the jet. As implied by the description given in Section 4, and confirmed by numerical experiments, this error behaves in a first-order way, i.e. doubling of the number of points across the nozzle reduces the percentage deviation by approximately half.

5.2 Collimation via a toroidal magnetic field – constant external pressure

For a first application of our code, we will study the effect of an increasingly strong toroidal magnetic field on the structure of an underexpanded jet propagating into an external medium of uniform pressure. As mentioned previously in Section 3, such a magnetic field could be responsible for the initial creation, stability and continued propagation of the jet.

There are four characteristic velocities associated with the flows under consideration here. These are:

(i) sound velocity $v_S = 1/\sqrt{3}$;
(ii) Alfvén wave velocity $v_A = [\beta/(2+\beta)]^{1/2}$;

(iii) fluid bulk velocity $v_{\rm jet}=[M_{\rm jet}^2/(2+M_{\rm jet}^2)]^{1/2}$, and
(iv) fast magnetosonic velocity $v_{\rm M}=[(c_{\rm S}^2+\Gamma_{\rm S}^2c_{\rm A}^2)/(1+c_{\rm S}^2+\Gamma_{\rm S}^2c_{\rm A}^2)]^{1/2}$.

All of these quantities can also be written in a quasi-Newtonian form (they can approach infinity and there is some formal similarity with the corresponding Newtonian equations when such quantities are used, see Königl 1980), i.e.

(i) sound velocity $c_{\rm S}=1/\sqrt{2}$;
(ii) Alfvén wave velocity $c_{\rm A}=(\beta/2)^{1/2}$;
(iii) fluid bulk velocity $c_{\rm jet}=M_{\rm jet}/\sqrt{2}$, and
(iv) fast magnetosonic velocity $c_{\rm M}=(c_{\rm S}^2+\Gamma_{\rm S}^2c_{\rm A}^2)^{1/2}$.

Note that $c_{\rm M}$ is a particular case of equation (45) in Königl (1980). Of course, the quasi-Newtonian quantities are not physical in the special relativity regime. From these expressions, it can be seen that for a flow to be super-Alfvénic only a modest Mach number is required, even if the magnetic field is extremely strong; i.e. $M_{\rm jet}^2\geq\beta$. Thus if $\beta=4$ we require only that $M_{\rm jet}\geq 2$. The relativistic Alfvén Mach number can be written as $M_{\rm A}=c_{\rm A}/c_{\rm S}=\sqrt{\beta}$. For our simulations typically $M_{\rm jet}\geq 10$, so the jets are always highly supermagnetosonic, at least close to the nozzle.

Initially, we take fixed parameter values of $1/\alpha^2=1.5$ and $M_{\rm jet}=10$. Then β is varied from $\beta=0$ (purely hydrodynamical) to $\beta=2$ (dominant magnetic field). In these cases, the pressure discontinuity is sufficiently weak that the jets do not produce shocks, even when the magnetic field is zero. The results of the calculations are shown in Figs 7(a)–(c). In Fig. 7(a), the jet radius is plotted as a function of distance along the z-axis. Even when no magnetic field is present the jet is well collimated, due to the existence of the constant-pressure external medium. The maximum radial expansion is only 20 per cent larger than the starting radius. In addition, it can be seen that a small toroidal field can substantially reduce the jet expansion. For $\beta>0.5$, the jet is

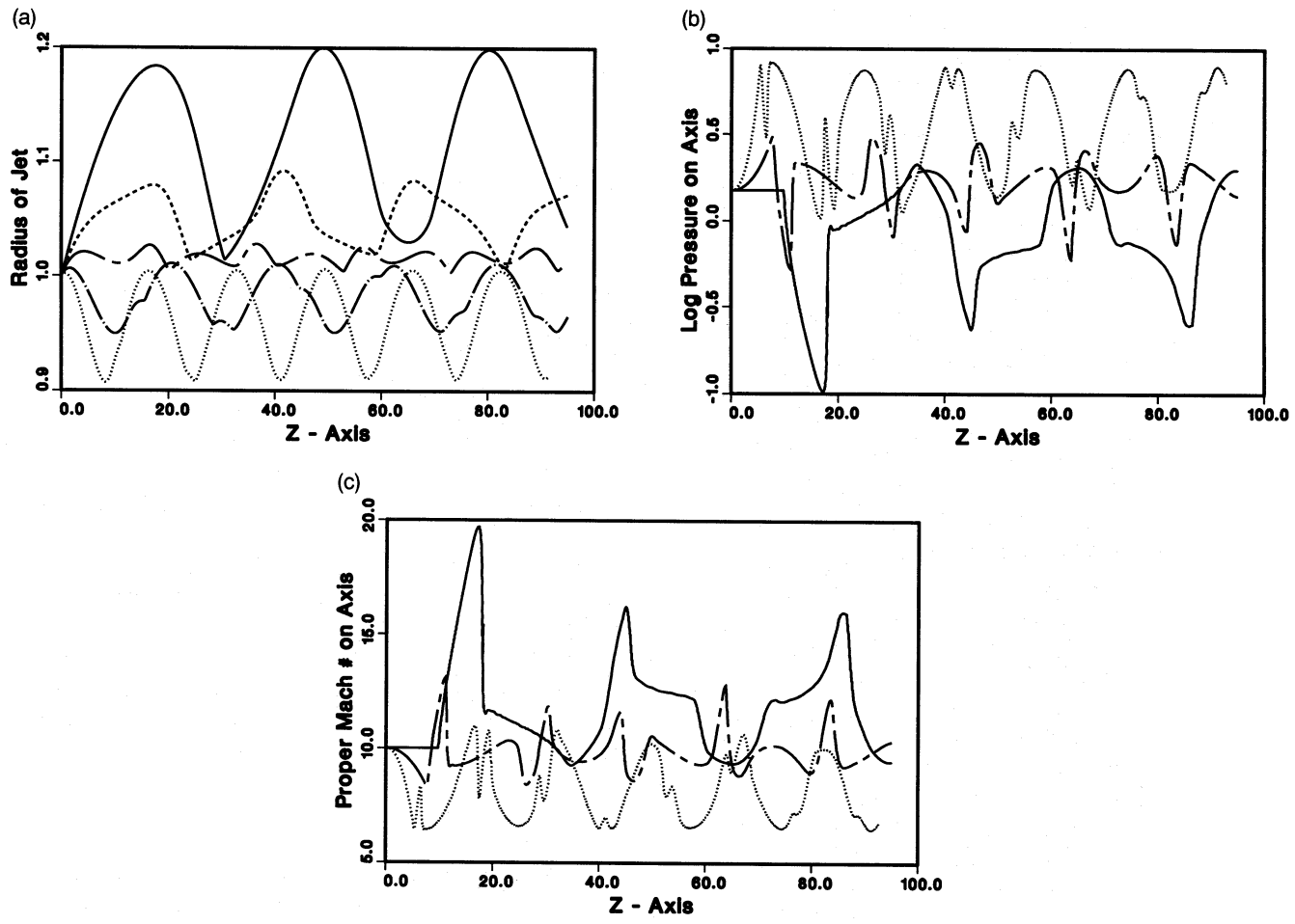

Figure 7. Results for a jet with $1/\alpha^2=1.5$ and $M_{\rm jet}=10$ for various values of β propagating into a constant-pressure external medium. (a) Suppression of the radial expansion of the jet due to an increasingly strong toroidal magnetic field. The values of β are denoted by: $\beta=0$ (solid line); $\beta=0.25$ (short-dashed line); $\beta=0.5$ (long-dashed–short-dashed line); $\beta=1$ (dot-dashed line); $\beta=2$ (dotted line). (b) Variation of the thermal pressure on the jet axis. (c) Variation of the Mach number on the jet axis. In (b) and (c), for clarity, only the values $\beta=0$, $\beta=0.5$ and $\beta=2$ are shown.

severely pinched and it contracts. The least variation in the jet boundary shape is produced when $\beta \sim 0.5$. As β increases, the jet oscillations become more frequent and the jet boundary shape more periodic. Thus portions of a jet with a strong toroidal magnetic field component could exhibit several very periodic bright features (e.g. knots), particularly since at such points the pressure on the axis is greatly enhanced and radio emission is likely to follow the fluid pressure. This pinch effect is clearly seen in Fig. 7(b), which plots the logarithm of the jet pressure on the z-axis. The external pressure is constant at $p_{\rm ext} = 1$. However, Fig. 7(c) shows that the bulk fluid velocity is reduced as the magnetic field strength increases and this would then reduce the relativistic beaming. The high-pressure regions work against collimation, but this is more than compensated for by the pinching effect of the toroidal field. In Fig. 8, we show contour plots for (a) the logarithm of the thermal pressure, (b) the logarithm of the Mach number, and (c) the magnetic pressure, for the case of $\beta = 2$. These plots clearly show the very periodic formation of islands of slowly moving, high-pressure gas pinched by an intense magnetic field.

From the results of these simulations, the following comments can be made about the effects of the toroidal magnetic field. When no field is present, the jet can have very large pressure and velocity changes along its length. From Fig. 7(a), when $\beta = 0$ the maximum z-axis pressure is approximately equal to that at the nozzle exit. On the other hand, the maximum Mach number (or equivalently Γ) can increase by a factor of 2. These variations decrease as β increases. The least variation in jet pressure and velocity occurs approximately for $\beta = 0.5$. Above this value, the jet radius decreases. When β is large, the thermal pressure on the z-axis can be much larger than the external pressure without decollimation occurring. Thus bright knots could be associated with a locally strong toroidal magnetic field. However, if a strong longitudinal magnetic field were present, this could work against collimation (Kössl et al. 1990c).

5.3 Collimation via a toroidal magnetic field – decreasing external pressure

A more realistic environment for astrophysical jets is one of an external medium with varying pressure distribution. X-ray data seem to indicate a general power-law fall-off in pressure with distance from the jet source, at least for elliptical galaxies (Schreier, Gorenstein & Feigelson 1982). Here we will investigate the effects of the toroidal magnetic field on the structure of the jet when it propagates into an external medium with a pressure distribution given by

$$p'(z) = \frac{p_{\rm ext}}{[1 + (z/z_{\rm core})^n]^{m/n}}. \tag{54}$$

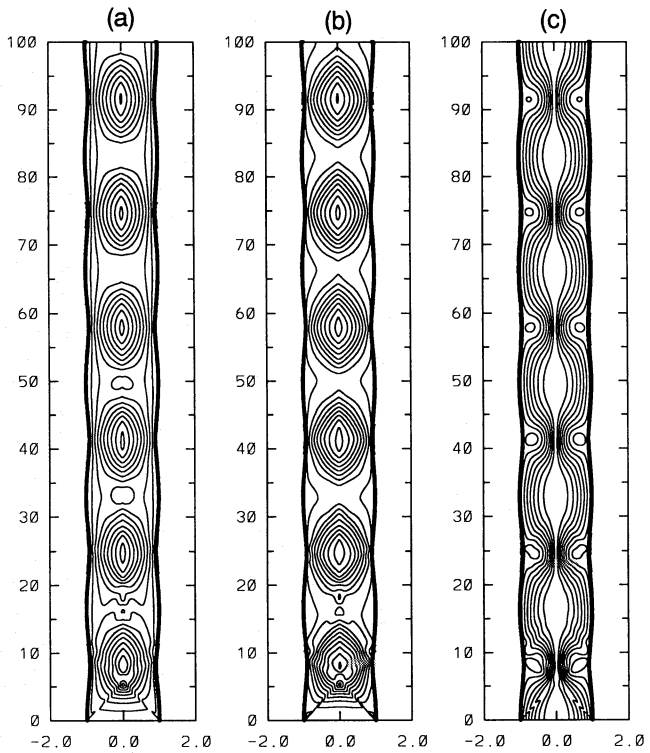

Figure 8. Contours of (a) logarithm of the thermal pressure [−0.140(0.087)1.088], (b) logarithm of the Mach number [0.849(0.022)1.158] and (c) the toroidal magnetic field strength [0.000(0.755)6.795] for the jet with $\beta = 2$. The notation used is [minimum level (increment) maximum level]. Note that these figures have been greatly expanded in the radial direction; the initial jet radius is $r_{\rm jet} = 1$.

This is similar to the pressure distribution used by Wilson & Falle (1985). Within the core radius, z_{core}, the external pressure is roughly constant, but outside it has a power-law fall-off of $p' \propto z^{-m}$. Typically $1 \leq m \leq 2$ and $z_{core} \sim$ a few jet radii.

In this investigation, the values of the parameters describing the underexpanded jets of the previous subsection will again be used, but this time with the external pressure given by (54). We will first take $z_{core} = 15$, $n = 4$ and $m = 2$; in this case, the external pressure drops sufficiently rapidly that a pure hydrodynamical jet will undergo free expansion (Wilson & Falle 1985). The range of β is again taken to be from $\beta = 0$ to $\beta = 2$. Figs 9(a)–(d) show the results of the simulations. Since the structures of these jets are much less periodic than those in a constant-pressure external medium, we have allowed them to propagate much further.

As expected, the $\beta = 0$ jet expands continuously, giving rise to a region of extremely low-pressure and high-velocity gas. This gas is quite strongly shocked, which brings it into near pressure equilibrium with the external medium (the pressure distribution of the external medium is shown as the thick solid line in Fig. 9b). There is no evidence of recollimation of the jet. In fact, from Fig. 9(a), it can be seen that no significant recollimation occurs for any value of β used here. This is because, as the jet expands and the external pressure decreases, the magnetic field strength is reduced and becomes less effective at pinching the plasma (see Fig. 9d). The magnetic field, however, does prevent shock formation and keeps the jet pressure substantially higher than that of the external medium. Moreover, when the toroidal field is very strong ($\beta > 2$), pressure perturbations at the nozzle are efficiently propagated downstream to produce a number of peaks in the z-axis pressure. Such jets would appear with bright knots of increasing separation (and decreasing brightness). In Figs 10(a)–(c), we show contours of (a) the logarithm of pressure, (b) the logarithm of the Mach number, and (c) the magnetic field strength for the $\beta = 2$ model.

We have repeated a similar experiment to the above, but this time with $z_{core} = 15$, $n = 4$ and $m = 1$, so that the external pressure drops as $p' \propto z^{-1}$. In this case, as can be seen from Figs 11(a)–(d), the periodic structure seen in the $p_{ext} =$ constant models reappears, particularly as β increases. Again, however, the jets continue to expand, although this time reconfinement shoulders do appear even in the $\beta = 0$ model. When $\beta = 0$, the jet pressure oscillates continuously about the external-pressure value. For $\beta > 0$, as in the previous case, the jet pressure is always much higher than the external pressure. In Figs 12(a)–(c), we show

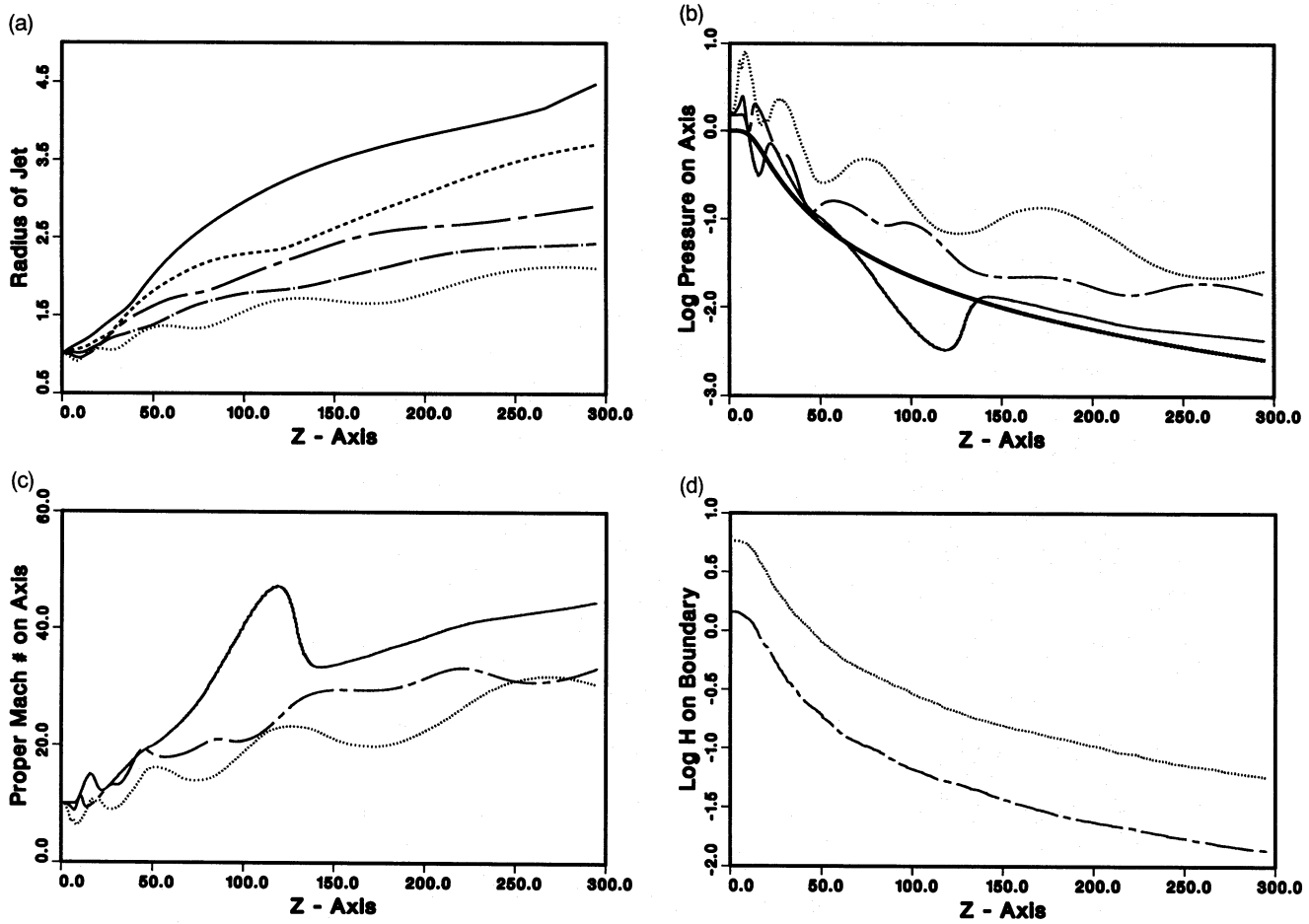

Figure 9. Results for a jet with $1/\alpha^2 = 1.5$ and $M_{jet} = 10$ for various values of β with the external pressure, p', given by (54). Here $n = 4$ and $m = 2$ so that $p' \propto z^{-2}$. Values of β are as indicated in Fig. 7. (a) Suppression of the radial expansion of the jet due to an increasingly strong toroidal magnetic field. (b) Variation of the thermal pressure on the jet axis (p' denoted by the thick solid line). (c) Variation of the Mach number on the jet axis. (d) The decay of the magnetic field on the jet boundary.

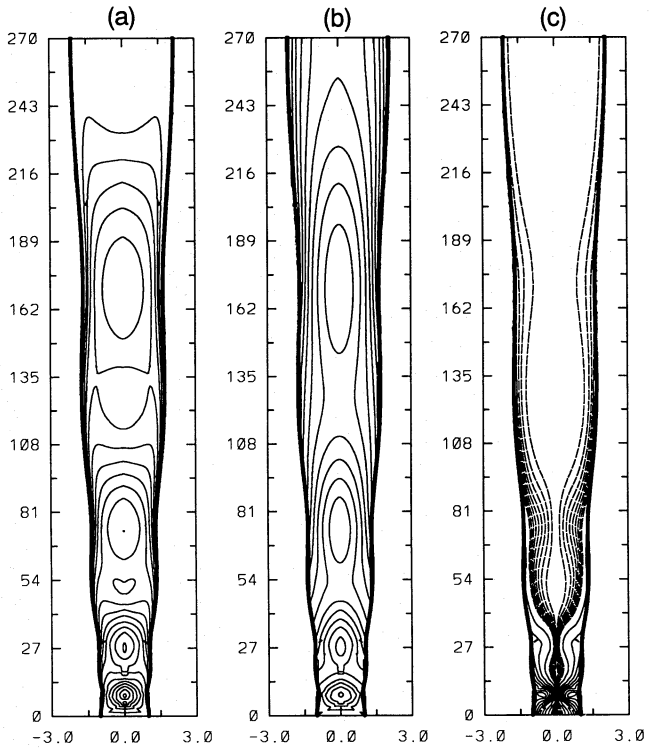

Figure 10. Contours of (a) logarithm of the thermal pressure [−1.500(0.131)1.000], (b) logarithm of the Mach number [0.850(0.052)1.850] and (c) the toroidal magnetic field strength [0.000(0.755)6.795] (solid line), [0.000(0.037)0.339] (dashed line) for the jet of Fig. 9 with $\beta = 2$. The notation is as in Fig. 8.

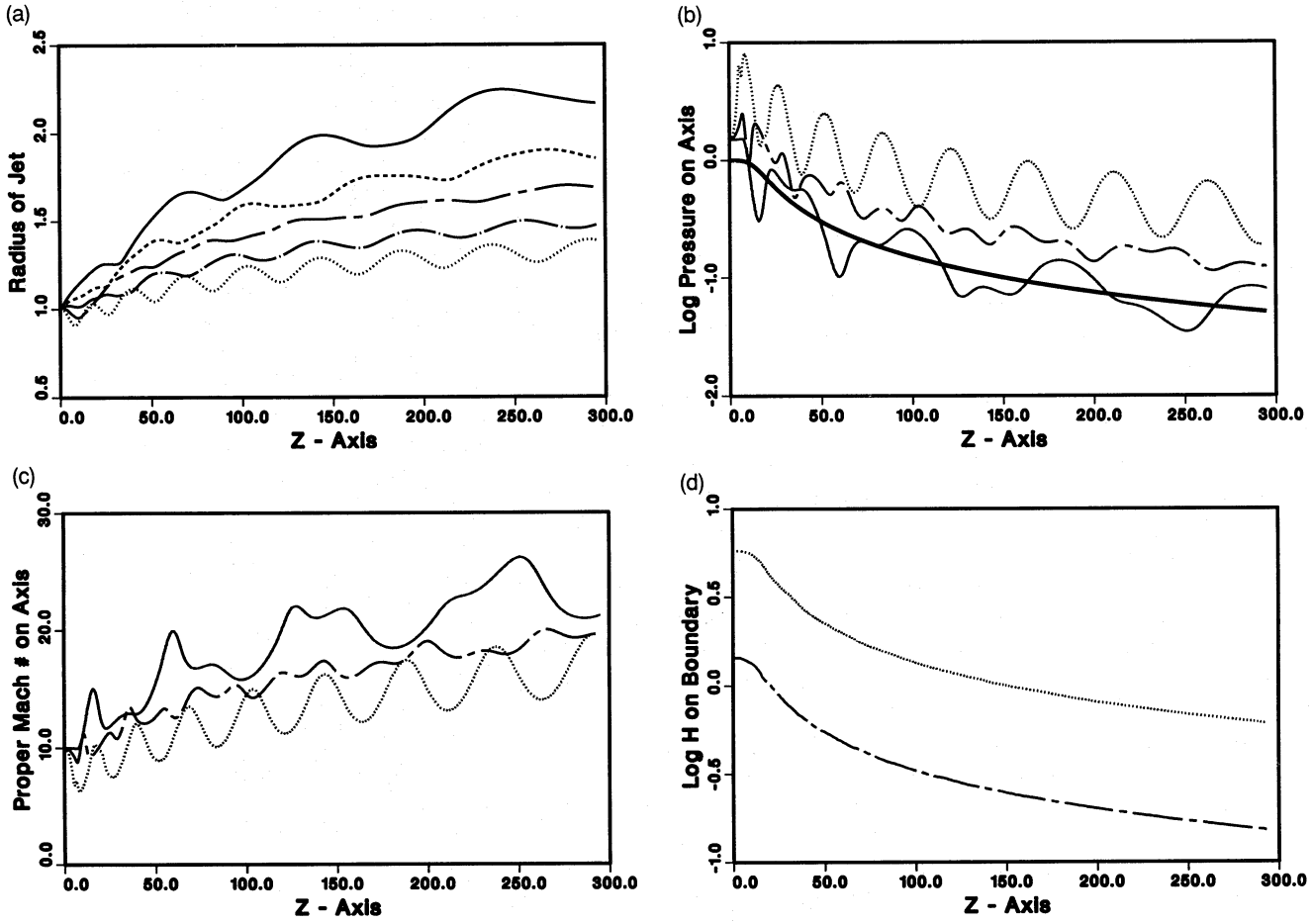

Figure 11. Results for a jet with $1/\alpha^2 = 1.5$ and $M_{\rm jet} = 10$ for various values of β with the external pressure, p', given by (54). Here $n = 4$ and $m = 1$ so that $p' \propto z^{-1}$. (a) Suppression of the radial expansion of the jet due to an increasingly strong toroidal magnetic field. Values of β are as indicated in Fig. 7. (b) Variation of the thermal pressure on the jet axis (p' denoted by the thick solid line). (c) Variation of the Mach number on the jet axis. (d) The decay of the magnetic field on the jet boundary.

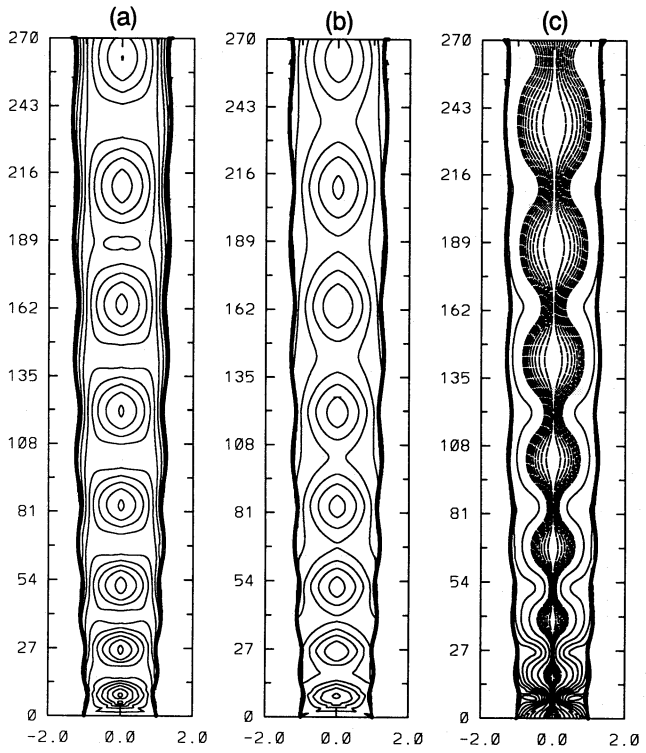

Figure 12. Contours of (a) logarithm of the thermal pressure [−1.500(0.131)1.000], (b) logarithm of the Mach number [0.850(0.052)1.850] and (c) the toroidal magnetic field strength [0.000(0.755)6.795] (solid line), [0.000(0.037)0.339] (dashed line) for the jet of Fig. 11 with $\beta=2$. The notation is as in Fig. 8.

contour plots of (a) the logarithm of pressure, (b) the logarithm of the Mach number, and (c) the magnetic field strength for the $\beta=2$ model.

6 CONCLUSIONS AND DISCUSSION

The previous results show aspects of steady relativistic MHD flows which may be of direct relevance to astrophysical jets, in particular compact radio jets which exhibit superluminal motion (Blandford & Königl 1979). No attempt has been made to model any specific observed jet since the physics we have used is far too simplified for detailed comparisons with observations. We can, however, make a number of general comments.

An important dynamical effect of the magnetic field is the reduction of the tendency for strong shock formation in the flow, although large pressure peaks still form when the jet reconfines. These high-pressure regions coincide with large toroidal magnetic field strengths and low bulk fluid velocities. As such, they would be identified with the bright knots in a jet, but, while the high pressure and magnetic field enhance synchrotron emission, beaming is reduced due to a lower Lorentz factor. The actual brightness of the knots in a synthesized radio map requires a correct treatment of the synchrotron radiation process taking into account beaming and line-of-sight effects (see e.g. Matthews & Scheuer 1990a,b). It is also of interest to note that, while the toroidal field can keep the jet pressure well above that of the external medium, it cannot stop the radial expansion of the jet when the external pressure drops. The rate of radial expansion, however, is reduced with increasing toroidal field strength.

The constant external pressure scenario is not a realistic one for astrophysical jets, but it illustrates an important phenomenon which persists when the external medium has varying pressure. As the toroidal field strength increases, the jet structure becomes more and more periodic. In addition, reconfinement and re-expansion of the jet occur on a shorter and shorter length-scale. This is due to the dynamics being taken over by the magnetic field, which has as its characteristic velocity the Alfvén wave speed. Then, as the magnetic field strength increases, this velocity approaches light speed.

When the external pressure varies as $p' \propto z^{-2}$, no periodic structures appear in the jet in the absence of a magnetic field. In this case, the jet ultimately reduces to a stream of gas with a very high Mach number (>40) in approximate pressure equilibrium with its surroundings and with an almost constant opening angle. This portion of the jet is unlikely to be visible. Moreover, there are no significant pressure enhancements anywhere, even close to the nozzle (see Fig. 9). None of this jet may therefore be visible. As the magnetic field strength is increased, the pressure perturbation, which is formed close to the nozzle by the pinching effect of the field, is propagated downstream with greater and greater efficiency. The first pressure peak is always the largest and

can be identified with the bright core of the jet. Subsequent pressure peaks could give rise to knots which probably decrease in brightness and have an increasing inter-knot distance moving out along the jet axis (see Fig. 9b). For a fixed pressure distribution of the external medium, the knots would increase in brightness and decrease in separation as the toroidal field strength increases. Moreover, additional knots could appear where none existed before.

If the external pressure $p' \propto z^{-1}$, some periodicity of the jet structure returns, particularly when the magnetic field strength is large. From Fig. 11, however, it is seen that there are many pressure peaks when $\beta = 2$. This would give rise to a large number of bright knots, and since there are no observations of this type it is unlikely that a combination of $p' \propto z^{-1}$ and $\beta \geq 2$ occurs in practice. The best parameters for observed jets seems to be around $p' \propto z^{-2}$ and $\beta \sim 2$. In any case, it may be possible to arrange the number, positions and brightnesses of knots in a jet using a simple combination of the external pressure distribution and the toroidal field strength in much the same way that Falle & Wilson (1985) did with the external pressure distribution to model specific knots in M87. This will be investigated in future work.

ACKNOWLEDGMENTS

We are very grateful to John Miller for reading the manuscript and making helpful suggestions for its improvement. This work was undertaken at SISSA, Trieste; Dipartimento di Fisica, Padova, and the Center for Relativity, Austin, Texas. We thank all of these institutions for their hospitality. MRD acknowledges the receipt of a NATO/SERC postdoctoral fellowship. Some of the computations in this paper were performed using the Cray Y-MP8/864 at the Center for High Performance Computing, University of Texas System, with Cray time supported by a Cray University Research grant to Richard Matzner. The Ministero Italiano per l'Università e la Ricerca Scientifica e Tecnologica is acknowledged for financial support. This work was supported in part by NSF Grant No. PHY-8806567.

REFERENCES

Anderson J. D., 1982, Modern Compressible Flow: With Historical Perspective. McGraw-Hill, New York
Anderson J. D., 1985, Fundamentals of Aerodynamics. McGraw-Hill, New York
Anile A. M., 1989, Relativistic Fluids and Magneto-fluids with Applications in Astrophysics and Plasma Physics. Cambridge Univ. Press, Cambridge
Anile A. M., Pennisi S., 1985, Ann. Inst. H. Poincaré, 46, 27
Appl S., Camenzind M., 1988, A&A, 206, 258
Benford G., 1987, in Kundt W., ed., Astrophysical Jets and their Engines. Reidel, Dordrecht, p. 197
Blandford R. D., Königl A., 1979, ApJ, 232, 34
Courant R., Friedrichs K. O., 1948, Supersonic Flows and Shock-waves. Springer-Verlag, New York
Daly R. A., Marscher A. P., 1988, ApJ, 334, 539
De Hoffman F., Teller E., 1950, Phys. Rev., 80, 692
Dubal M. R., 1991, Comput. Phys. Commun., 64, 221
Falle S. A. E. G., 1987, in Kundt W., ed., Astrophysical Jets and their Engines. Reidel, Dordrecht, p. 151
Falle S. A. E. G., 1991, MNRAS, 250, 581
Falle S. A. E. G., Wilson M. J., 1985, MNRAS, 216, 79
Ferrari A., Trussoni E., Zaninetti L., 1981, MNRAS, 196, 1051
Hoskin N. E., 1963, in Methods of Computational Physics, Vol. 3. Academic Press, New York, p. 265
Illingworth C. R., 1953, in Howarth L., ed., Modern Developments in Fluid Dynamics: High Speed Flow, Vol. 1. Oxford Univ. Press, Oxford, p. 105
Kennel C. F., Coroniti F. V., 1984, ApJ, 283, 694
Königl A., 1980, Phys. Fluids, 23, 1083
Kössl D., Müller E., Hillebrandt W., 1990a, A&A, 229, 378
Kössl D., Müller E., Hillebrandt W., 1990b, A&A, 229, 397
Kössl D., Müller E., Hillebrandt W., 1990c, A&A, 229, 401
Lichnerowicz A., 1967, Relativistic Hydrodynamics and Magneto-hydrodynamics. Benjamin, New York
Lind K. R., Payne D. G., Meier D. L., Blandford R. D., 1989, ApJ, 344, 89
Matthews A. P., Scheuer P. A. G., 1990a, MNRAS, 242, 616
Matthews A. P., Scheuer P. A. G., 1990b, MNRAS, 242, 623
Moe M. M., Troesch B. A., 1960, Am. Rocket Soc., 30, 487
Norman M. L., Winkler K.-H. A., 1984, in Winkler K.-H. A., Norman M. L., eds, Astrophysical Radiation Hydrodynamics. Reidel, Dordrecht, p. 187
Owczarek J. A., 1964, Fundamentals of Gas Dynamics. International Textbook Co., Scraton
Sanders R. H., 1983, ApJ, 266, 75
Schreier E. J., Gorenstein P., Feigelson E. D., 1982, ApJ, 261, 42
Sloan J. H., Smarr L. L., 1987, in Centrella J. M., LeBlanc J., Bowers R., eds, Numerical Astrophysics. Jones and Bartlett, Boston, p. 52
Wardle J. F. C., Potash R. I., 1982, in Heeschen D. S., Wade C. M., eds, Proc. IAU Symp. 97, Extragalactic Radio Sources. Reidel, Dordrecht, p. 129
Wilson M. J., 1984, MNRAS, 209, 923
Wilson M. J., 1987a, MNRAS, 224, 155
Wilson M. J., 1987b, MNRAS, 226, 447
Wilson M. J., Falle S. A. E. G., 1985, MNRAS, 216, 971
Zensus J. A., Pearson T. J., 1987, Superluminal Radio Sources. Cambridge Univ. Press, Cambridge